SCIENTIFIC REPORTS

OPEN

Enhanced proton acceleration from an ultrathin target irradiated by laser pulses with plateau ASE

Dahui Wang[1,2], Yinren Shou[1], Pengjie Wang[1], Jianbo Liu[1], Chengcai Li[1], Zheng Gong[1], Ronghao Hu[1], Wenjun Ma[1] & Xueqing Yan[1,3]

We report a simulation study on proton acceleration driven by ultraintense laser pulses with normal contrast (10^7–10^9) containing nanosecond plateau amplified spontaneous emission (ASE). It's found in hydrodynamic simulations that if the thickness of the targets lies in the range of hundreds nanometer matching the intensity and duration of ASE, the ablation pressure would push the whole target in the forward direction with speed exceeding the expansion velocity of plasma, resulting in a plasma density profile with a long extension at the target front and a sharp gradient at the target rear. When the main pulse irradiates the plasma, self-focusing happens at the target front, producing highly energetic electrons through direct laser acceleration(DLA) building the sheath field. The sharp plasma gradient at target rear ensures a strong sheath field. 2D particle-in-cell(PIC) simulations reveal that the proton energy can be enhanced by a factor of 2 compared to the case of using micrometer-thick targets.

Proton acceleration by the interaction of ultraintense, ultrashort laser pulses with matter has obtained high energy and short duration proton beams[1,2]. For applications in the fields of medical therapy, inertial confinement fusion (ICF), material irradiation effects and proton imaging[3,4], several acceleration schemes including target normal sheath acceleration (TNSA)[5–8], radiation pressure acceleration (RPA)[9–11], and break-out after burner (BOA)[12,13] were widely studied. In these schemes, the presence of nanosecond ASE pedestal leaked from the regenerative amplifier can significantly influence the acceleration process. Many researches have studied the effects on different mechanisms of ion acceleration by ASE theoretically and experimentally[14–19]. For a typical Ti:sapphire laser, the ASE has a contrast of 10^7–10^9 and duration of a few nanosecond. Under the interaction of ASE, a preplasma will be created at the target front[20–24]. Meanwhile, the shock launched by the ASE, after propagating through the target, will give rise to an expanding plasma at the rear side of the target[17,25–27]. It is found that the preplasma normally contributes positively to the acceleration as it enhances the laser absorption[16,28–32], but the plasma at the rear side of the target, even with μm scale length, can significantly reduce the sheath field[33–37]. As a result, the presence of ASE in most cases is harmful to proton acceleration. Several techniques such as plasma mirrors[38,39], optical parametric chirped pulse amplification (OPCPA) technique[40] and plasma shutters[41] have been employed to suppress ASE. But most of them take the price of energy loss for the laser pulses.

In this letter, we report on the proton acceleration by irradiating targets using normal contrast (10^7–10^9) laser pulses[15] containing nanosecond plateau amplified spontaneous emission (ASE). We found in hydrodynamic simulations[42] that if the thickness of target was in the range of hundreds nanometer, the plasma gradient at the target rear was unexpectedly short compared to micrometer-thick targets. Relativistic PIC simulations[43] revealed that the maximum proton energy obtained from these ultrathin targets was 2 times as much as that of micrometer-thick target. This result can be explained that for ultrathin targets, the displacement resulting from ablation pressure of ASE exceeds the forward expansion of the plasma at the target rear. As a result, the plasma density profile becomes asymmetry, and a density spike, still overdense meanwhile, moves forwardly as a whole. In this case, the plasma gradient at the rear surface of the moving target is very short, which is highly favorable to proton acceleration. Systematic study reveals that the optimal target thickness depends on the ASE intensity. At the optimal thickness, the dependence of the maximum proton energy on the main pulse intensity was also investigated.

[1]State Key Laboratory of Nuclear Physics and Technology, Peking University, Beijing, 100871, China. [2]State Key Laboratory of Laser Interaction with Matter, Northwest Institute of Nuclear Technology, Xi'an, 710024, China. [3]Collaborative Innovation Center of Extreme Optics, Shanxi University, Taiyuan, Shanxi, 030006, China. Dahui Wang and Yinren Shou contributed equally to this work. Correspondence and requests for materials should be addressed to W.M. (email: wenjun.ma@pku.edu.cn) or X.Y. (email: x.yan@pku.edu.cn)
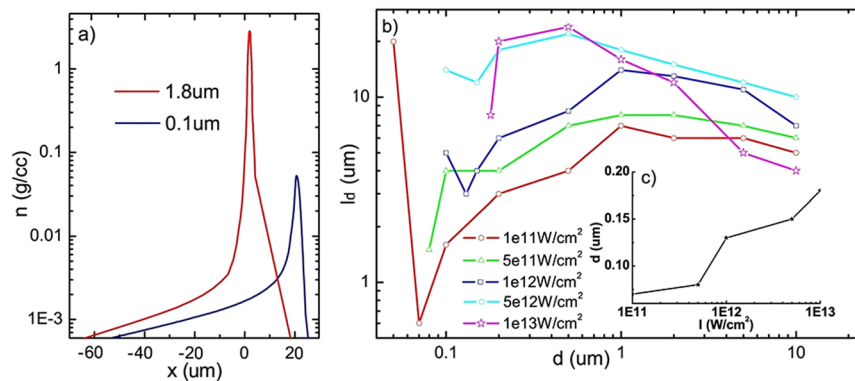
Figure 1. (**a**) The plasma density profiles from MULTI simulations for different thickness of targets irradiated by ASE at intensity of 10^{12} W/cm^2. The red line and blue line are the results of 1.8 μm and 0.1 μm respectively. The laser originates from the left side. (**b**) Plasma gradient scale length at the target rear versus the thickness of the target irradiated by different ASE intensity. (**c**) The dependence of optimal target thickness with minimum gradient scale length on ASE intensity.
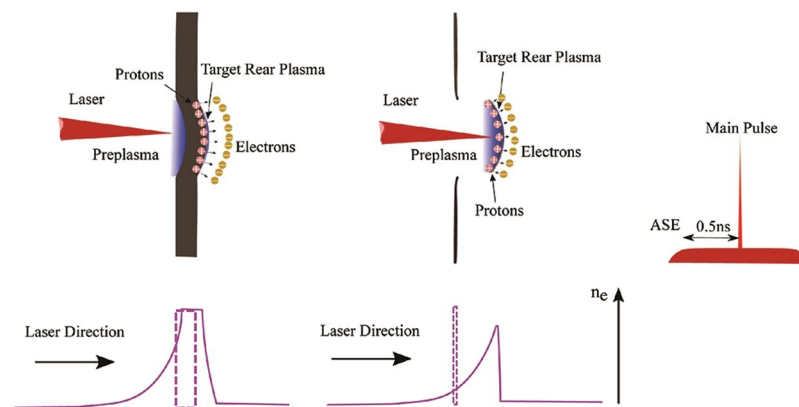

Figure 2. Schematic of proton acceleration by 0.1 μm and 1.8 μm target interaction with laser pulse containing ASE.

Results

Hydrodynamic simulations were performed to study the evolution of the targets under irradiation of ASE. The ASE was set such that the pulse duration is 0.5 ns and the intensity ranges from 10^{11} W/cm^2 to 10^{13} W/cm^2. Figure 1(a) shows the plasma density distribution along the laser direction at intensity of 10^{12} W/cm^2 for aluminum target with thickness of 0.1 μm and 1.8 μm. The density profile at the front of the targets can be expressed by $n_e = n_c exp\left(\frac{x - x_c}{l_f}\right)$ for $x < x_c$, where n_c is the critical density, x_c the position of critical-density layer, and l_f the scale length of the plasma at the target front. The density distribution at the target rear can be described by the formula $n_e = n_0 exp\left(-\frac{l_r}{l_d}\right)$[44], where l_r is the distance away from the unperturbed region, l_d is plasma scale length at the target rear. l_f and l_d are both crucial to the proton acceleration. It was reported that the optimal thickness of the targets, at which the combination of l_f and l_d was optimal for proton acceleration, was 3.6 $\mu m/ns \times \tau_{ASE}$ in previous study[16]. Therefore, we chose a 1.8 μm thick target matching our 0.5 ns ASE as a comparison to 0.1 μm targets. By fitting obtained density profiles in the simulations, it's found that l_f/l_d of 0.1 μm and 1.8 μm targets is 62/2.5 μm and 52/15 μm respectively. Although l_f of the two cases are similar, the difference of l_d is drastic. To systematically investigate the influence of ASE on l_d, we varied the ASE intensity I_{ASE} and performed serials of simulations. l_d is shown as a function of d for different I_{ASE} in Fig. 1(b), where d is the thickness of the target. It's found that for a given I_{ASE}, there was an optimal thickness in the range of a few hundreds nanometer, where l_d is minimal. This optimal thickness linearly scales up with the increment of ASE intensity as shown in Fig. 1(c). The value of l_d at the optimal thickness scales up the intensity of ASE with a minimal value of 0.6 μm for 0.07 μm targets.

Figure 2 schematically illustrates the acceleration process for the cases of ultrathin and micrometer-thickness foils irradiated by the laser pulses with plateau ASE. For a micrometer-thick target, preplasma with scale length of tens of micrometer is formed at the target front, in together with deformation and a plasma with sufficient extension at the target rear. The whole target has a small displacement. In the case of hundreds-nanometer-thin target, preplasma with similar scale length is formed at the target front. However, the whole target move a long
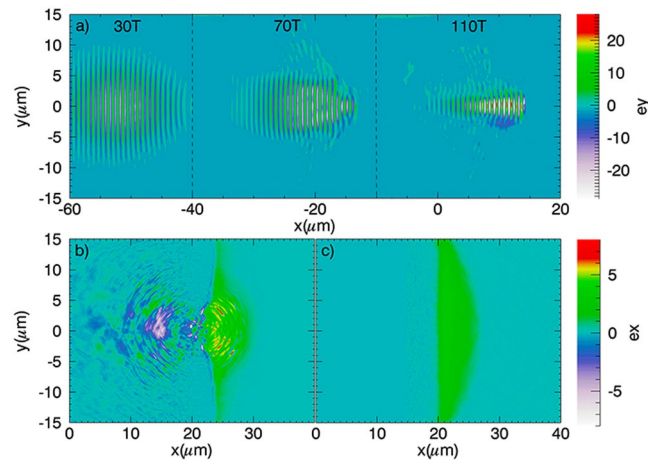
Figure 3. (**a**) The normalized laser electric field Ey at 30 T, 70 T and 110 T. The maximum normalized electric field Ex of 0.1 μm (**b**) and 1.8 μm (**c**) targets respectively. The origin targets before ASE locate at the position of x = 0.
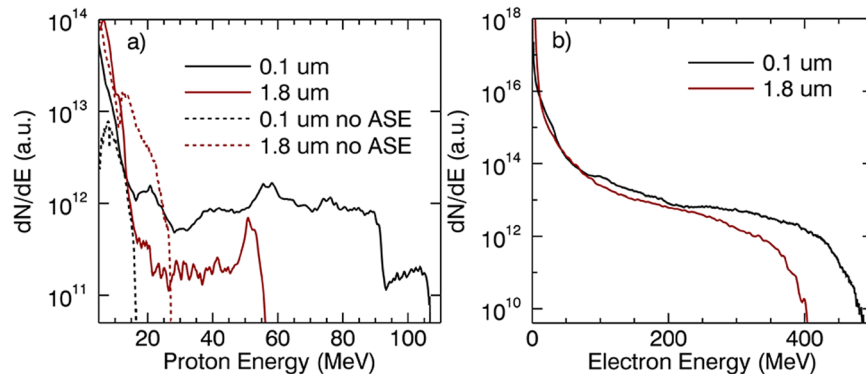

Figure 4. (**a**) Proton energy spectra of 0.1 μm and 1.8 μm targets with and without ASE at 250 T. (**b**) The electron energy spectra of 0.1 μm and 1.8 μm targets with ASE at 120 T.

distance along the laser direction with a smaller scale length plasma at the target rear. After the ASE, the main pulses interact with the expanded plasma at the target front and generate hot electrons. When these electrons leave the targets, a sheath field is established at the rear side of the targets. The scale length of plasma at both sides of the targets will impose significant influence on the strength of the sheath field.

To illustrate the acceleration process of protons in the sheath field, 2D PIC simulations with parameters of plasma density distribution, and electron/proton temperatures obtained from hydrodynamic simulations were performed. In the simulations, the main laser is circularly polarized and has a Gaussian envelope. The laser normalized intensity, spot focus size, and duration were set as 12 (corresponding to a peak laser intensity of $3.08 \times 10^{20} \, W/cm^2$), 6 μm and 10 T respectively, where $T = 2.67 \, fs$ is the laser period. The transverse and longitudinal electric fields obtained from simulations for 0.1 μm and 1.8 μm targets for the case of with ASE are depicted in Fig. 3. Relativistic self-focusing and laser intensity enhancement can be observed in both cases as shown in Fig. 3(a). The maximum enhancement factor of laser amplitude is 4.2 for the 1.8 μm target, which is slightly larger than that of 4 for the 0.1 μm target. In spite of stronger self-focusing, the maximum sheath electrostatic field at the rear side of the 1.8 μm target is significantly weaker than that for the 0.1 μm target as shown in Fig. 3(b). The proton energy spectra are shown in Fig. 4(a). The maximum proton energy for the 0.1 μm and 1.8 μm target is about 107 MeV and 56 MeV at 250 T respectively. As an interesting comparison, we also performed simulations for the same targets without ASE. it's found that the values of maximum proton energy for both targets are significantly lower compared to the cases of with ASE.

Discussion

The density profile of the target after the interaction of ASE plays a key role in the ion acceleration. For the 0.1 μm and 1.8 μm targets under the irradiation of nanoseconds ASE, the areal density of the region before the critical density plasma is very small compared to the bulk targets. Thus, we can employ hydrodynamic analytical theories to illustrate the physics and reveal the dependence of density profile on the ASE intensity and duration as below. When the ASE irradiates a target, the plasmas at the target front will expand due to the absorption of laser energy.

Here, l_f can be determined by $l_f = c_s t$, where c_s is the sound velocity of the expanding plasma. The c_s can be expressed by $c_s \approx 0.31 \times 10^6 \sqrt{\frac{T_e}{keV}} \sqrt{\frac{Z}{A}}$[45], where Z and A are effective ion charge and the mass number. For the ASE intensity of $10^{11} \sim 10^{13} W/cm^2$, $T_e(eV) = \left(\frac{I_{ASE}}{10^4 W/cm^2} \left(\frac{\lambda}{\mu m} \right)^2 \right)^{2/3} eV$. Meanwhile, a strong shock is launched and travels quickly through the target. The shock has the velocity of $v_s = \sqrt{(\gamma+1)\frac{P_s}{\rho_0}}$[25], where γ is the adiabatic constant, ρ_0 is the density of the target, and $P_s(Mbar) = 8.6 \left(\frac{I_{ASE}}{10^{14} W/cm^2} \right)^{2/3} \lambda^{-2/3} \left(\frac{A}{2Z} \right)^{1/3}$ is the shock pressure. If the target is thin enough that the shock can arrive at the target rear and break out within the ASE duration, a rarefaction wave will be created. The target will be ionized in a very short time by the rarefaction wave and form a dense plasma moving forwardly driven by the shock pressure. In an overall point of view, the target is pushed as a whole by the shock pressure of ASE. For simplicity, the mean velocity of the target can be approximately given by $v_{target} \approx \frac{1}{2} \frac{P_s}{\rho_0 d} \left(\tau_{ASE} - \frac{d}{v_s} \right)$[25], where d is the thickness of the target. After the interaction of ASE, the displacement of the target is $x \approx \left(\tau_{ASE} - \frac{d}{v_s} \right) \times v_{target}$.

Based on the above analysis, the condition that leads to the formation of an plasma density profile with a long extension at the target front and a sharp gradient at the target rear after the ASE would be

$$x > c_s \tau_{ASE}. \tag{1}$$

In this case, the whole target will catch up with the plasma and 'strike' it. Accordingly, a plasma density profile of the target after the ASE, with a sharp plasma gradient at the target rear, will be formed. By plugging in the expression of c_s and x, we can get:

$$d \leq \frac{P_s \tau_{ASE}}{2\rho_0 c_s \left(1 + \frac{1}{v_s} \right)}. \tag{2}$$

Accordingly, there is a critical target thickness of $d_c = d_c = \frac{P_s \tau_{ASE}}{2\rho_0 c_s \left(1 + \frac{1}{v_s} \right)}$ where the regime just takes place. Take ASE intensity of $10^{12} W/cm^2$, $\tau_{ASE} = 0.5 ns$ and $\lambda = 800 nm$ as an example, P_s and c_s are about $0.41 Mbar$ and $30 km/s$ respectively. For the Al target, we obtain $d \approx 0.13 \mu m$. The $0.1 \mu m$ target meets the demand of forming an symmetric plasma density profile. Detailed evolution of the plasma density profiles for the $0.1 \mu m$ target was investigated by hydrodynamic simulations. Results show that l_d increases in a very short time. Then, the peak density of the target drops quickly and the position of density peak starts to move forward. Meanwhile, a plasma density profile with a long extension at the target front and a sharp gradient at the target rear is formed. l_d begins to decrease until $t = 0.5 ns$. For the $1.8 \mu m$ target, the thickness of the target is much larger than d_c, and the displacement of the target is very small compared to $c_s \tau_{ASE}$. As a result, in contrast to the case of $0.1 \mu m$ target, the density profile of $1.8 \mu m$ target has a large l_d under the irradiation of ASE as shown in Fig. 1(a).

The displacement of the targets under ablation pressure also has important influence on l_f. The relationship can be expressed as $l_f \approx x + c_s \tau_{ASE}$. In the condition of the same laser parameters, x of the $0.1 \mu m$ and $1.8 \mu m$ targets are calculated as $20 \mu m$ and $0.3 \mu m$ respectively. This explains why l_f of $0.1 \mu m$ target with the value of $62 \mu m$ is slightly large than that of the $1.8 \mu m$ target, in spite of similar expansion velocity of the preplasma at the target front. The validity of 1D hydrodynamic simulation results is testified by MULTI 2D by using a Gaussian laser. We found that plasma scale length at the rear side of $0.1 \mu m$ target in the center of the Gaussian laser beam is also significantly smaller than that of $1.8 \mu m$ target in spite of different deformation due to the laser intensity distribution.

The preplasma resulting from the ASE has huge influence on the proton acceleration. When interacting with the preplasma at the target front, the main laser pulse experiences relativistic self-focusing due to the spatiotemporal variation of the refractive index and a long-living channel is formed as shown in Fig. 3(a). The radius of the focused laser spot size can be estimated as $r = \frac{1}{\pi} \sqrt{\frac{a_0 n_c}{\sqrt{2} ne}}$[28,29,33–35,46], where n_e is the initial electron density. The n_e of the $0.1 \mu m$ and $1.8 \mu m$ targets is about $0.37 n_c$ and $0.4 n_c$ respectively, calculated as the mean density of the preplasma by the method of area integral. For our simulation parameters, this gives the laser spot size value of $1.55 \mu m$ and $1.5 \mu m$, consistent with the simulation results ($1.52 \mu m$ and $1.45 \mu m$). In addition, the preplasma length of the two targets approach to the self-focusing length with the value of $55 \mu m$ shown in 3(a). This ensures an efficient self-focusing. When the self-focusing happens, the laser amplitude is enhanced, such as in our cases, by a factor of 4 and 4.2 for the two types of targets. At the same time, the energetic electrons are efficiently accelerated by the direct laser acceleration (DLA)[47–49]. The temperature of the DLA electrons can be described as $T_e = 1.5(I_{main}\lambda^2/13.8GW)^{1/2}$, where I_{main} is the intensity of the main pulse. The maximum energy of the DLA electrons is more than 400 MeV as shown in Fig. 4(b). This is obviously larger than the electrons accelerated by the ponderomotive potential described as $T_e = 0.5[(1 + (I_{main}\lambda^2/13.8GW)/2)^{1/2} - 1]$[28,29,33,46]. These DLA electrons have high energy density. When they arrive at the target rear, a stronger and stable sheath field is bulit, resulting in a higher proton energy compared to the case of without ASE.

We note that the maximum proton energy of $0.1 \mu m$ target is about twice as much as that of $1.8 \mu m$ target with presence of ASE. The two targets have the similar preplasma profile at the target front, resulting in almost the same relativistic self-focusing and laser intensity enhancement. However, plasma scale length at the rear side of $1.8 \mu m$ target is significantly larger than $0.1 \mu m$ target. To explain this result, the proton acceleration mechanism of the $0.1 \mu m$ target needs to be considered. In Fig. 4(a), the protons show a plateau energy spectrum[10,33,50], which can be judged as TNSA mechanism in previous works. To verify the scheme, a serial of 2D simulations with different intensity of the main laser pulses were performed. Figure 5(a) shows the dependence of maximum
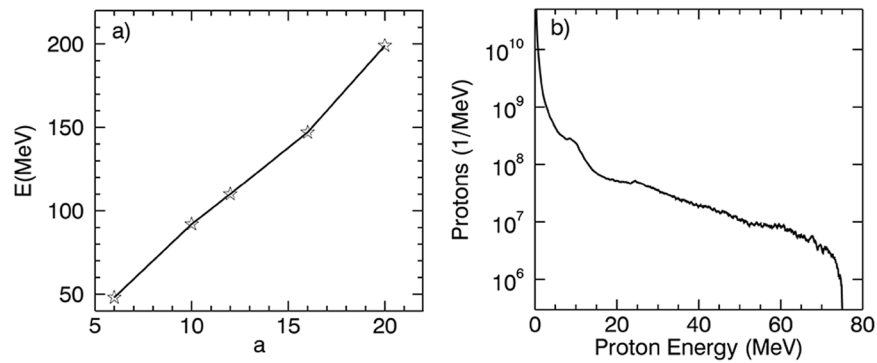
Figure 5. (**a**) The scaling law between the proton energy and the laser intensity. (**b**) Proton energy spectra of a $0.1 \mu m$ target obtained from 3D simulations.

proton energy on the laser amplitude. The scaling can be approximately described as $E \propto I^{1/2}$, which also shows a remarkable signature of TNSA mechanism in another aspect. For TNSA mechanism of proton acceleration, the maximum proton energy is determined by the sheath electrostatic field at the target rear. The strength of the field can be described as $k_B T_e/(e\lambda_D)$, where k_B, e, and λ_D are Boltzmann constant, charge of the electrons, and the Debye length respectively. If the plasma pre-expansion is negligible, the sheath field will be reduced to $k_B T_e/(e l_d)$[17]. Since l_d of the $0.1 \mu m$ target is significantly smaller than that of the $1.8 \mu m$ target, the maximum proton energy obtained from the $0.1 \mu m$ targets is consequently higher.

For a more precise prediction of proton energy, 3D PIC simulations with the same plasma density and laser parameters were performed. The proton energy spectra is shown in Fig. 5(b). The maximum energy of the protons is 70 MeV, lower than the results in 2D simulations. The difference of the maximum proton energy between the 2D and 3D simulations is due to the 3D effect. For example, the electrons beam expansion spatial angle is 2π in 2D but 4π in 3D space; the sheath field in 3D simulations will be lower owing to the faster expansion of the electrons. All these are overlooked in 2D simulations.

In conclusion, we have demonstrated the enhanced proton acceleration from hundreds nanometer target irradiated by a normal contrast (10^7–10^9) laser pulse containing nanosecond plateau ASE. It is shown in 2D simulations that protons with the energy more than 100 MeV can be generated by a Gaussian CP laser pulse at the intensity of $3.08 \times 10^{20} W/cm^2$ interacting with a $0.1 \mu m$ aluminum target. Compared to the case using $1.8 \mu m$ targets, the maximum proton energy is 2 times higher. We reveal that such enhancement is due to the plasma profile with a long extension at the target front and a sharp gradient at the target rear created by the plateau ASE. It provides an efficient way to obtain high energy protons for the wide applications in the condition of laser containing nanosecond plateau ASE, instead of employing complicated methods to increase the contrast. We should emphasize that the scheme is verified for the main pulses with plateau ASE. The extendibility of our conclusions to other types of ASE with prepulses or exponential rising edge needs to be further studied.

Methods

Hydrodynamic Simulations. Hydrodynamic code MULTI was employed to obtain the evolution and the density distribution of the targets irradiated by the ASE. The ASE pulse has the duration $\tau_{ASE} = 0.5\,ns$, intensity ranging from $10^{11}\,W/cm^2$ to $10^{13}\,W/cm^2$ and wavelength $\lambda = 0.8\,\mu m$. The material of the targets is aluminum and its initial density ρ_0 is $2.7\,g/cm^3$.

PIC Simulations. PIC simulations of the proton acceleration for Al targets with the thickness of $0.1\,\mu m$ and $1.8\,\mu m$ were performed at the cases of presence and absence of ASE. The fully relativistic 2D PIC code, EPOCH, was used. Each simulation was defined with Cartesian spatial dimensions of $100\,\mu m \times 30\,\mu m$ using 12000×600 computational mesh cells. A circularly polarized laser pulse with a Gaussian envelope $a = a_0 \exp\left(-\frac{(x-x_0)^2}{r_0^2}\right)\exp\left(-\frac{(t-t_0)^2}{\tau^2}\right)$ irradiates the target normally from the left side. The laser parameters a_0, x_0, r_0, t_0, and τ are set as 12 (corresponding to a peak laser intensity of $3.08 \times 10^{20}\,W/cm^2$), $0, 6\,\mu m, 20\,T$ and $10\,T$ respectively, where $T = 2.67\,fs$ is the laser period. The targets in simulations were Aluminum materials with the initial density of $2.7\,g/cm^3$. We set the target two ion species (aluminum ions and protons) with the ratio of 10:1. Simulations of the ion acceleration for the target with the thickness of 0.1 um and 1.8 um are performed at the cases of low-contrast and high-contrast laser (with and without ASE pedestal). The boundaries of the simulation box are all defined as free space. The laser enters from the left boundary. 3D PIC simulations with box size of $100\,\mu m \times 30\,\mu m \times 30\,\mu m$ sampled by $5000 \times 450 \times 450$ grids were performed.

References

1. Borghesi, M. *et al.* Fast ion generation by high-intensity laser irradiation of solid targets and applications. *Fusion Sci. Technol.* **49**, 412–439 (2006).
2. Clark, E. *et al.* Measurements of energetic proton transport through magnetized plasma from intense laser interactions with solids. *Phys. Rev. Lett.* **84**, 670 (2000).
3. Roth, M. *et al.* Fast ignition by intense laser-accelerated proton beams. *Phys. Rev. Lett.* **86**, 436 (2001).
4. Bulanov, S., Esirkepov, T. Z., Khoroshkov, V., Kuznetsov, A. & Pegoraro, F. Oncological hadrontherapy with laser ion accelerators. *Phys. Lett. A* **299**, 240–247 (2002).

5. Snavely, R. *et al*. Intense high-energy proton beams from petawatt-laser irradiation of solids. *Phys. Rev. Lett.* **85**, 2945 (2000).

6. Wilks, S. *et al*. Energetic proton generation in ultra-intense laser–solid interactions. *Phys. Plasmas* **8**, 542–549 (2001).

7. Passoni, M. & Lontano, M. Theory of light-ion acceleration driven by a strong charge separation. *Phys. Rev. Lett.* **101**, 115001 (2008).

8. Fuchs, J. *et al*. Laser-driven proton scaling laws and new paths towards energy increase. *Nat. Phys.* **2**, 48 (2008).

9. Macchi, A., Veghini, S. & Pegoraro, F. 'light sail' acceleration reexamined. *Phys. Rev. Lett.* **103**, 085003 (2009).

10. Bulanov, S. *et al*. Enhancement of maximum attainable ion energy in the radiation pressure acceleration regime using a guiding structure. *Phys. Rev. Lett.* **114**, 105003 (2015).

11. Dollar, F. *et al*. Finite spot effects on radiation pressure acceleration from intense high-contrast laser interactions with thin targets. *Phys. Rev. Lett.* **108**, 175005 (2012).

12. Albright, B. *et al*. Relativistic buneman instability in the laser breakout afterburner. *Phys. Plasmas* **14**, 094502 (2007).

13. Yin, L. *et al*. Three-dimensional dynamics of breakout afterburner ion acceleration using high-contrast short-pulse laser and nanoscale targets. *Phys. Rev. Lett.* **107**, 045003 (2011).

14. Wagner, F. *et al*. Accelerating ions with high-energy short laser pulses from submicrometer thick targets. *High power laser science and engineering* **4**, 1 (2016).

15. Hiroyuki Daido, a. M. N. & Pirozhkov, A. S. Review of laser-driven ion sources and their applications. *Reports on progress in physics* **75**, 056401 (2012).

16. Kaluza, M. *et al*. Influence of the laser prepulse on proton acceleration in thin-foil experiments. *Phys. Rev. Lett.* **93**, 045003 (2004).

17. Fuchs, J. *et al*. Laser-foil acceleration of high-energy protons in small-scale plasma gradients. *Phys. Rev. Lett.* **99**, 015002 (2007).

18. Cai, H. *et al*. Prepulse effects on the generation of high energy electrons in fast ignition scheme. *Phys. Plasmas* **17**, 023106 (2010).

19. Glinec, Y., Genoud, G., Lundh, A., Persson, A. & Wahlström, C. Evolution of energy spectrum from laser-accelerated protons with a 100 fs intense prepulse. *Appl. Phys. B* **93**, 317 (2008).

20. Andreev, A. *et al*. Effect of a laser prepulse on fast ion generation in the interaction of ultra-short intense laser pulses with a limited-mass foil target. *Plasma Phys. Contr. F.* **48**, 1605 (2006).

21. Zhao, S. *et al*. Ion acceleration enhanced by target ablation. *Phys. Plasmas* **22**, 073106 (2015).

22. Ovchinnikov, V. *et al*. Effects of preplasma scale length and laser intensity on the divergence of laser-generated hot electrons. *Phys. Rev. Lett.* **110**, 065007 (2013).

23. Lin, X. *et al*. Effect of prepulse on fast electron lateral transport at the target surface irradiated by intense femtosecond laser pulses. *Phys. Rev. E* **82**, 046401 (2010).

24. Debayle, A., Honrubia, J., d'Humieres, E. & Tikhonchuk, V. Divergence of laser-driven relativistic electron beams. *Phys. Rev. E* **82**, 036405 (2010).

25. Batani, D. *et al*. Effects of laser prepulses on laser-induced proton generation. *New J. Phys.* **12**, 045018 (2010).

26. Benware, B., Macchietto, C., Moreno, C. & Rocca, J. J. Demonstration of a high average power tabletop soft x-ray laser. *Phys. Rev. Lett.* **81**, 5804 (1998).

27. Lee, H., Pae, K., Suk, H. & Hahn, S. Enhancement of high-energy ion generation by preplasmas in the interaction of an intense laser pulse with overdense plasmas. *Phys. Plasmas* **11**, 1726 (2004).

28. Wilks, S., Kruer, W., Tabak, M. & Langdon, A. Absorption of ultra-intense laser pulses. *Phys. Rev. Lett.* **69**, 1383 (1992).

29. Antici, P. *et al*. Measuring hot electron distributions in intense laser interaction with dense matter. *New J. Phys.* **14**, 063023 (2012).

30. Flacco, A. *et al*. Characterization of a controlled plasma expansion in vacuum for laser driven ion acceleration. *Joural of Applied Physics* **104**, 103304 (2008).

31. Nuter, R. *et al*. Influence of a preplasma on electron heating and proton acceleration in ultraintense laser-foil interaction. *Joural of Applied Physics* **104**, 103307 (2008).

32. Mckenna, P. *et al*. Effects of front surface plasma expansion on proton acceleration in ultraintense laser irradiation of foil targets. *Laser Part. Beams* **26**, 591 (2008).

33. Wang, H. *et al*. Efficient and stable proton acceleration by irradiating a two-layer target with a linearly polarized laser pulse. *Phys. Plasmas* **20** (2013).

34. Pukhov, A., Sheng, Z.-M. & Meyer-ter Vehn, J. Particle acceleration in relativistic laser channels. *Phys. Plasmas* **6**, 2847–2854 (1999).

35. Bin, J. *et al*. Ion acceleration using relativistic pulse shaping in near-critical-density plasmas. *Phys. Rev. Lett.* **115**, 064801 (2015).

36. Lindau, F. *et al*. Laser-accelerated protons with energy-dependent beam direction. *Phys. Rev. Lett.* **95**, 175002 (2005).

37. Lundh, O., Lindau, F., Persson, A. & Wahlström, C. Influence of shock waves on laser-driven proton acceleration. *Phys. Rev. E* **76**, 026404 (2007).

38. Doumy, G. *et al*. Complete characterization of a plasma mirror for the production of high-contrast ultraintense laser pulses. *Phys. Rev. E* **69**, 026402 (2004).

39. Hörlein, R. *et al*. High contrast plasma mirror: spatial filtering and second harmonic generation at $10^{19} wcm^{-2}$. *New J. Phys.* **10**, 083002 (2008).

40. Dubietis, A., Jonušauskas, G. & Piskarskas, A. Powerful femtosecond pulse generation by chirped and stretched pulse parametric amplification in bbo crystal. *Opt. Comm.* **88**, 437–440 (1992).

41. Esirkepov, T. Z. *et al*. Proposed double-layer target for the generation of high-quality laser-accelerated ion beams. *Phys. Rev. lett.* **89**, 175003 (2002).

42. Ramis, R., Schmalz, R. & Meyer-ter Vehn, J. Multi-a computer code for one-dimensional multigroup radiation hydrodynamics. *Comput. Phys. Commun.* **49**, 475–505 (1988).

43. Sheng, Z.-M., Mima, K., Zhang, J. & Sanuki, H. Emission of electromagnetic pulses from laser wakefields through linear mode conversion. *Phys. Rev. Lett.* **94**, 095003 (2005).

44. Yogo, A. *et al*. Laser ion acceleration via control of the near-critical density target. *Phys. Lett. E* **77**, 016401 (2008).

45. Rödel, C. *et al*. High repetition rate plasma mirror for temporal contrast enhancement of terawatt femtosecond laser pulses by three orders of magnitude. *Appl. Phys. B* **103**, 295–302 (2011).

46. Wagner, F. *et al*. Maximum proton energy above 85 mev from the relativistic interaction of laser pulses with micrometer thick ch 2 targets. *Phys. Rev. Lett.* **116**, 205002 (2016).

47. Macchi, A., Borghesi, M. & Passoni, M. Ion acceleration by superintense laser-plasma interaction. *Reviews of Modern Physics* **85**, 751 (2013).

48. Robinson, A., Arefiev, A. & Khudik, V. The effect of superluminal phase velocity on electron acceleration in a powerful electromagnetic wave. *Phys. Plasmas* **22**, 083114 (2015).

49. Jiang, S. *et al*. Microengineering laser plasma interactions at relativistic intensities. *Phys. Rev. Lett.* **116**, 085002 (2016).

50. Yuan, F. *et al*. Combined proton acceleration from foil targets by ultraintense short laser pulses. *Plasma Phys. Contr. F.* **58**, 045025 (2016).

Acknowledgements

Author Contributions

Additional Information

Competing Interests: The authors declare no competing interests.

Publisher's note: Springer Nature remains neutral with regard to jurisdictional claims in published maps and institutional affiliations.